X-ray spectroscopy for chemistry in the 2-4 keV energy regime at the XMaS beamline: ionic liquids, Rh and Pd catalysts in gas and liquid environments, and Cl contamination in γ-Al₂O₃

Paul B. J. Thompson,[a,b]* Bao N. Nguyen,[c] Rachel Nicholls,[c] Richard A. Bourne,[c] John B. Brazier,[d] Kevin R. J. Lovelock,[d] Simon D. Brown,[a,b] Didier Wermeille,[a,b] Oier Bikondoa,[a,e] Christopher A. Lucas,[b] Thomas P. A. Hase[e] and Mark A. Newton[e]*

[a]XMaS, UK CRG, ESRF, 71 Avenue des Martyrs, 38043 Grenoble, France, [b]Department of Physics, University of Liverpool, Oliver Lodge Laboratory, Liverpool L69 7ZE, UK, [c]School of Chemistry, University of Leeds, Leeds LS2 9JT, UK, [d]Department of Chemistry, Imperial College London, South Kensington Campus, London SW7 2AZ, UK, and [e]Department of Physics, University of Warwick, Gibbet Hill Road, Coventry CV4 7AL, UK.
*Correspondence e-mail: pthompso@esrf.fr, m.newton.2@warwick.ac.uk

The 2–4 keV energy range provides a rich window into many facets of materials science and chemistry. Within this window, P, S, Cl, K and Ca K-edges may be found along with the L-edges of industrially important elements from Y through to Sn. Yet, compared with those that cater for energies above ca. 4–5 keV, there are relatively few resources available for X-ray spectroscopy below these energies. In addition, in situ or operando studies become to varying degrees more challenging than at higher X-ray energies due to restrictions imposed by the lower energies of the X-rays upon the design and construction of appropriate sample environments. The XMaS beamline at the ESRF has recently made efforts to extend its operational energy range to include this softer end of the X-ray spectrum. In this report the resulting performance of this resource for X-ray spectroscopy is detailed with specific attention drawn to: understanding electrostatic and charge transfer effects at the S K-edge in ionic liquids; quantification of dilution limits at the Cl K- and Rh L₃-edges and structural equilibria in solution; in vacuum deposition and reduction of [Rh¹(CO)₂Cl]₂ to γ-Al₂O₃; contamination of γ-Al₂O₃ by Cl and its potential role in determining the chemical character of supported Rh catalysts; and the development of chlorinated Pd catalysts in 'green' solvent systems. Sample environments thus far developed are also presented, characterized and their overall performance evaluated.

1. Introduction.

X-ray absorption fine-structure (XAFS) spectroscopy is now a core technique for many areas of research and especially where deriving element-specific chemical state and local structure information under conditions of application are at a premium. For the most part such studies are carried out at energies in the ca. 4–30 keV energy range as this is where the K-edges of the majority of the commonly studied elements are found along with L₃-edges of elements >Cs. As a result, the vast majority of operational X-ray resources are optimized for this energy range and there are relatively few that offer the possibility of high-energy XAFS (>30 keV) or indeed XAFS down to ca. 2 keV.

As with the high-energy XAFS regime (Ghigna & Spinolo, 2015), the 2–4 keV range is in many ways highly attractive to many areas of research, and resources capable of such studies

100 mm travel linear translation for sample changer

Huber High precision XYZ mount +/- 3mm

SSD 150mm² Detector

Incident Beam

Motorised retractable feedthrough

Chamber sits on stand designed for 4 Tesla Magnet

Extra ports for "dosing" or mass spectrometer
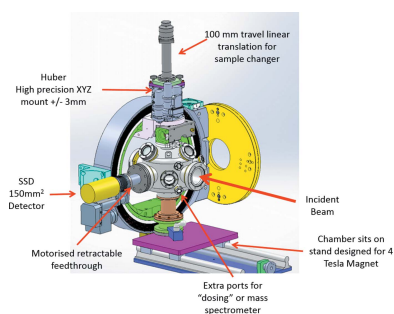
are to be found at many synchrotrons. A non-exhaustive list might include: 9BM (Advanced Photon Source, USA), 4.3 and 14.3a (Stanford, USA), 8BM (in development at NSLS-II, Brookhaven), I811 (MAXlab, Sweden), B18 and I18 (Diamond Light Source, UK), Lucia (Soleil, France), ID26, ID12 and ID21 (ESRF, France) and Phoenix (Swiss Light Source, Switzerland). Nonetheless, operational capacity in this energy regime, as compared with the *ca.* 4–30 keV range, is, by comparison, considerably smaller and therefore even more at a premium given the range of researchers and research disciplines that compete for it.

The *K*-edges of elements such as P, S and Cl, which are of intrinsic interest in the biological sciences, geosciences and many areas within chemistry, are to be found within this region of the X-ray spectrum.

The L_3-edges of numerous important elements, including the Group 5 transition metals, also exist in this range. For the most part these elements are studied at their higher-energy *K*-edges, but this is not to say that there is no merit to be found in addressing them from their L_3-edges. Issues of reduced lifetime broadening, that can effectively limit the insight attainable in higher-energy XANES experiments, are much reduced and *L*-edge studies are intrinsically more sensitive to chemical changes than their deeper *K*-edge counterparts.

Further, in many situations, *i.e.* coordination and organometallic chemistry as well as catalysis, being cases in point, elements such as Cl, P and S can often be found (as ligands, promoters or poisons) within the same chemical system as 5*d* transition metal elements. Whilst it is often possible to obtain some information about these lower-*Z* elements from the (metal) *K*-edge XAFS derived from higher-energy experimentation, this information does not address issues of speciation and structure (particularly electronic) of the lower-*Z* element directly. In addition, and again catalysis contains many examples, these low-*Z* elements can have profound effects upon the properties of functional materials that may be expressed even at levels at which they are simply not possible to observe clearly from the perspective of high-energy edges.

Moreover, other techniques that may be sensitive to aspects of speciation and structures of S, P and Cl, such as NMR, infrared and Raman spectroscopy, also have their own limitations in sensitivity or operation (for instance, high temperatures). As such, determining the behaviour of what are often adjunct elements to the overall formulation of a functional materials can be a challenging task. There is, therefore, considerable merit in studying such systems from the perspective of the *K*-edges of the S, P, Cl and the *L*-edges of the metals in question using XAFS: XAFS has no intrinsic temperature limit to its application and, at third-generation synchrotrons equipped with up-to-date detectors, has a potentially very competitive limit to its sensitivity.

That said, lower X-ray energies pose challenges to *in situ* or *operando* study that are significantly ameliorated at higher energies. These principally arise from the increased scattering and absorption events that lower-energy X-rays will be subject to, that result in a much reduced ability to penetrate matter. Developing methods (see, for instance, Tamenori, 2010, 2013;

Tamenori *et al.*, 2011) or sample environment suitable for the study of any given process at these energies is therefore subject to considerably more constraints (both in terms of design and materials) than is the case at high energies. However, several examples exist for the study of gas–solid chemistry and catalysis (see, for example, van der Eerden *et al.*, 2000; Hayter *et al.*, 2002; Dathe *et al.*, 2005; Nurk *et al.*, 2013; Bolin *et al.*, 2013; König *et al.*, 2014) and studies using a liquid media (Brown *et al.*, 2012; Fulton *et al.*, 2012; Pin *et al.*, 2013).

The XMaS beamline at the ESRF was originally conceived as an instrument to study X-ray magnetic scattering (Paul *et al.*, 1995; Brown *et al.*, 2001) and is situated on the soft end of an ESRF dipole magnet (critical energy = 9.8 keV). At this time there was much interest in the scattering community for actinide magnetism (see, for example, Isaacs *et al.*, 1989) and for resonant diffraction at the U M_5 absorption edge (~3.55 keV). Over the last five years XMaS has been substantially upgraded to increase the X-ray flux at low energies (currently to 2.4 keV). Fig. 1 shows resulting improvements in X-ray throughput calculated using *XOP* (Del Rio & Dejus, 2004) for a focused 0.5 mm^2 beam.

Much progress has also been made in developing in-vacuum sample environments to minimize absorption due to windows and air gaps. As detailed in Fig. 1, these upgrades have resulted in gains of over three orders of magnitude of available flux at 3.1 keV, with still greater gains at softer energies (Thompson *et al.*, 2010).

One major driving force behind these new developments, and within the original remit of the beamline, was the desire to study resonant scattering at the *L*-edges of 4*f* rare-earth elements and at *K*-edges down to sulfur. As a result, XMaS
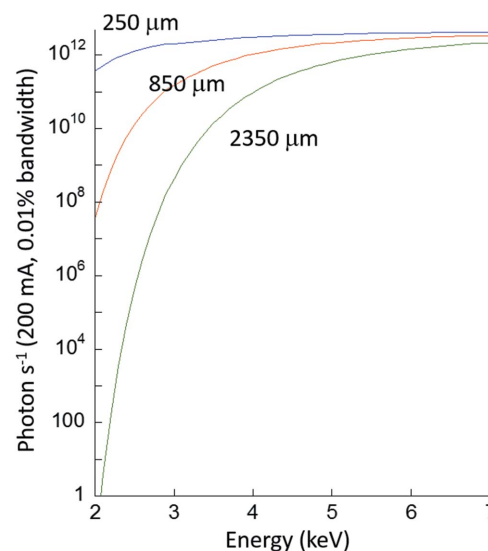
Figure 1
Flux [calculated using *XOP* (Del Rio & Dejus, 2004)] plotted as a function of photon energy from the XMaS beamline. The green curve represents a typical experimental setup with a cryostat, incorporating beryllium vacuum and radiation shields. The red curve shows the flux of the original beamline configuration of 850 μm of beryllium; the blue curve shows the flux with the new front-end and removable beryllium window.

has developed a niche for the delivery of high-intensity low-energy photons in the 2–4 keV energy range. Latterly this capacity has recently attracted the interest of a potentially large and diverse chemistry community. Within materials chemistry in general there is much interest in understanding local chemical environments of elements such as S, Cl and P using K-edge X-ray spectroscopies such as XANES and EXAFS; this community also has significant interest in the L-edges of the second-row transition metal elements and row 5 of the periodic table in general [Y (L_3 = 2.07 keV) to I (L_3 = 4.557 keV)].

The requirements of X-ray spectroscopy, irrespective of, but in some ways compounded by, a focus on soft X-ray energies, are somewhat different to those of X-ray scattering measurements. It cannot be guaranteed, therefore, that beamline optics designed for the latter can offer an optimal, or even viable, solution to achieve the former. This report therefore aims to critically assess the performance of the current XMaS beamline for spectroscopy in the 2–4 keV range using a number of prototypical examples of important materials classes such as ionic liquids and catalysts. In the latter case we give examples of application to gas–solid and liquid–solid systems and detail the sample environments developed for the *in situ* study of working materials and processes at these energies.

2. Technical aspects of the beamline in relation to soft X-ray spectroscopy

The XMaS beamline was originally conceived to provide a high-flux, tunable, focused X-ray source for the purpose of resonant X-ray diffraction and takes a 3.0 mrad fan of radiation horizontally from the ESRF bending magnet. To prevent any possible contamination of the ESRF storage ring there is a 250 μm-thick beryllium window in the front-end of the beamline. The first optical element is a fixed-exit water-cooled Si $\langle 111 \rangle$ monochromator, situated 24.5 m from the source. The main axis of the monochromator is driven by a DC servo motor that has a precision and reproducibility of $\sim 0.0001°$, essential for the energy scans required in typical X-ray resonant scattering experiments. An ESRF-designed water-cooled first crystal is used to initially monochromate the beam. Cooling is achieved *via* a series of tubes close to the diffracting surface of the first crystal. A constant vertical offset of 20 mm with respect to the white beam is provided by a second un-cooled Si $\langle 111 \rangle$ crystal, mounted within an in-house-designed crystal cage. This second crystal is mounted *via* a kinematic mount onto three high-precision linear actuators, with a step resolution of 50 nm. These three actuators allow the distance between the two crystals to be changed, thus maintaining a constant offset. In addition, this three-point kinematical design facilitates the alignment of the second crystal, as both pitch and roll motions are achieved by simply adjusting the appropriate actuators. This design allows the distance between the two crystals to be changed easily as the energy is changed and then aligned when the energy is initially fixed.

The distance between the two crystals is not changed during a typical energy scan, as the cyclic pitch error on the three actuator screw threads means that the Bragg condition on the second crystal is not met due to the small angular changes as the height is changed. For most of the resonant scattering measurements generally performed on XMaS, this has not been problematic as the energy range scanned has been, at most, 100 eV around an absorption edge. If we take an example of looking at an energy scan of ± 50 eV at 9 keV, the change of the calculated distance between the two crystals is only 6 μm. However, when working at lower energies, the monochromator Bragg angles become a lot larger, as does the distance between the first and second crystals required to maintain a constant beam offset. For example, if we look at an energy scan from 2.8 keV to 3.23 keV, the change in distance between the two crystals is nearly 1.5 mm to maintain a constant offset. This distance becomes considerably larger at lower energies. If the monochromator is used in a 'channel-cut' mode, this will lead to a large vertical displacement of the beam after the monochromator.

The primary focusing mirror used on XMaS is a 1.2 m-long rhodium-coated toroid at 4.5 mrad, so all of the beams arriving at the mirror should be theoretically focused onto the same focal spot. Therefore the vertical acceptance of the mirror helps to mitigate the effects of the vertical beam offset at the focal point of the beam.

The availability of harmonic rejection mirrors on the XMaS beamline helps greatly in performing low-energy measurements. These mirrors, originally designed over ten years ago, have been primarily used for performing resonant scattering where the energy range of any energy scans is generally limited to 100 eV. This energy range is acceptable for XANES which at these energies will most likely be the principle occupation of the studies. The length of these Pyrex mirrors is 350 mm and half of the surface of the Pyrex is coated with a rhodium stripe to allow for the transmission of higher-energy X-rays when the mirror is translated laterally across the beam. Typically, for energies below 3 keV, the angle of incidence used for the Pyrex mirrors is around 6.5 mrad, cutting off radiation above 5 keV. When performing a long low-energy scan of 300 eV, this means that, currently, the beam is overflowing from the mirrors and they are essentially acting as a slit, as the beam is displaced vertically.

2.1. Detectors and monitors

Both the detector and the monitors used for the studies made here are silicon drift diodes (SDD). The monitor consists of a Vortex silicon drift diode mounted onto a vacuum flange that is exposed to the scatter of the incident X-rays from a Kapton foil. It was found to be advantageous to use the same type of detector for the monitor as well as the main fluorescence detector in order to correctly normalize the rhodium absorption dip from the primary mirror. Initially the primary fluorescence detector was another Vortex silicon drift diode with an active area of 50 mm^2, but this has recently been upgraded to a Ketek 150 mm^2 silicon drift diode (energy

resolution $\simeq$ 160 eV). The output of the main fluorescence detector is connected to a Mercury XIA digital signal processor which was used with a 4096-channel multichannel analyser (MCA).

3. Sample environment for XAFS in the 2–4 keV energy range

3.1. Overall experimental arrangement

As the XMaS beamline was originally designed to perform high-resolution single-crystal diffraction, the heart of the instrument is a large six-circle Huber diffractometer that permits scattering in both horizontal and vertical planes (Paul *et al.*, 1995; Brown *et al.*, 2001). This multi-circle diffractometer is mounted on a large high-precision table that can support heavy loads, such as superconducting magnets weighing up to 150 kg. This table has both vertical and transverse translations with respect to the beam.

As such, and for low-energy spectroscopy and chemical studies, a new stainless steel vacuum vessel has been constructed that can fit within the Eulerian cradle of this diffractometer. This arrangement is shown schematically in Fig. 2.

This chamber allows a vacuum or a helium atmosphere (essential for such low-energy studies) to be maintained around the samples or sample environment to be used as well as providing ports for the fluorescence detector, dosing of molecules (see below), mounting of a mass spectrometer, or other additional elements required for an experiment such as, for example, a light source. It also provides a path for transmission studies (for instance, small-angle X-ray scattering or transmission XAFS at higher energies) to be made within the same experiment if desired.
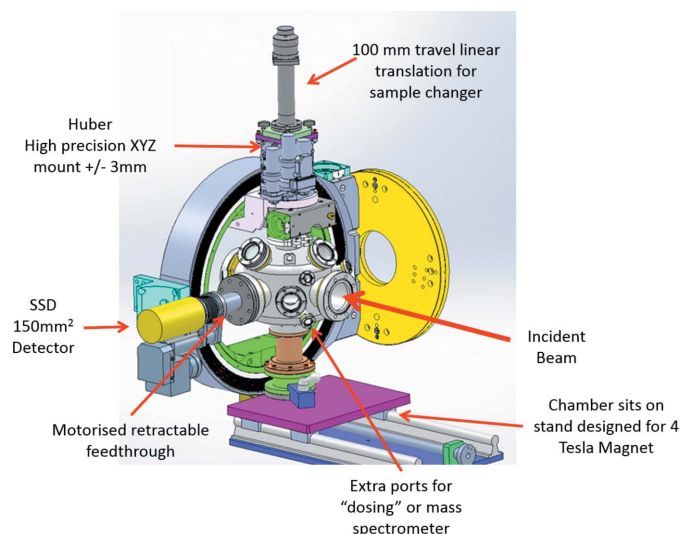
Figure 2
Schematic of the generic environmental chamber designed and used for the low-energy spectroscopic studies outlined in this paper, illustrating how it fits within the six-circle Huber diffractometer, the geometry of the fluorescence yield XAFS experiments, and other salient aspects of the experimental flexibility it engenders.

Samples, or indeed entire sample environments, each of these discussed later in this paper sit inside this chamber, are mounted onto a precision XYZ carrier (Huber) that can fit within the Φ circle of the diffractometer. Onto this carrier can be mounted cryostats and cryo-furnaces with a temperature range from 2 to 800 K. Cryogenic systems are based on closed-cycle helium refrigeration, such as the APD DE-202 displex head. A sample-changer system based on a VG linear vacuum drive mounted onto the Huber precision cryostat carrier is also available which enables up to ten samples to be loaded at one time.

3.2. Cell for soft X-ray spectroscopy studies of liquids and liquid–solid chemistry

The study of chemistry occurring in the liquid phase, or which requires a liquid phase in contact with a solid phase, is, in a number of ways, more demanding than the gas–solid systems for which the previously described sample environment was initially developed. Liquid–solid catalysis is especially important for the synthesis of fine chemicals but also in a variety of fields such as electrochemistry, geochemistry and biology. Moreover, in recent years the use of flow, rather than static or batch systems, has become considerably more important for applied processes (Hartman *et al.*, 2011; Ley, 2012; Newman & Jensen, 2013).

A liquid is considerably more absorbing than an equivalently thick layer of gas. Therefore, and especially at low X-ray energies, its presence constrains both elements of the design and the materials that may be used. Increased X-ray absorption also increases the potential for deleterious effects that arise from the use of low-energy X-rays such as local heating and/or the generation of electrons and radical species. As a result the use of flowing liquids, rather than static, might also be seen as a pre-requisite such that these potential issues are minimized.

When using a liquid, a window is also, by and large, a pre-requisite. This, combined with the materials available for these energies, and that they be very thin, also means that vacuum cannot be used. Instead, a He atmosphere between the sample cell and the detector is required.

Figs. 3 and 4 show a first design for a cell derived for studying liquids or liquid–solid systems in a single-pass flow arrangement and using a fluorescence yield geometry. As before, it is designed to sit within the general-purpose chamber outlined above (Fig. 2) and therefore can be very precisely aligned within the six-circle diffractometer in place on the XMaS beamline. Liquid flow is provided using a syringe driver, connected externally, that pumps liquid to the cell itself *via* the 1/8″ Swagelok connections. The sample sits within a 100 μm-deep trench across which the liquid flows. Depending upon the solid sample to be used, a stainless steel mesh (Goodfellow) is placed in the sample recess and used to retain the sample that is pressed within it (Sherborne *et al.*, 2015). However, if the sample cannot be pressed into such a mesh (as in the examples of Pd/Al$_2$O$_3$ catalysts given below), it was found that the best solution to retaining the sample bed in
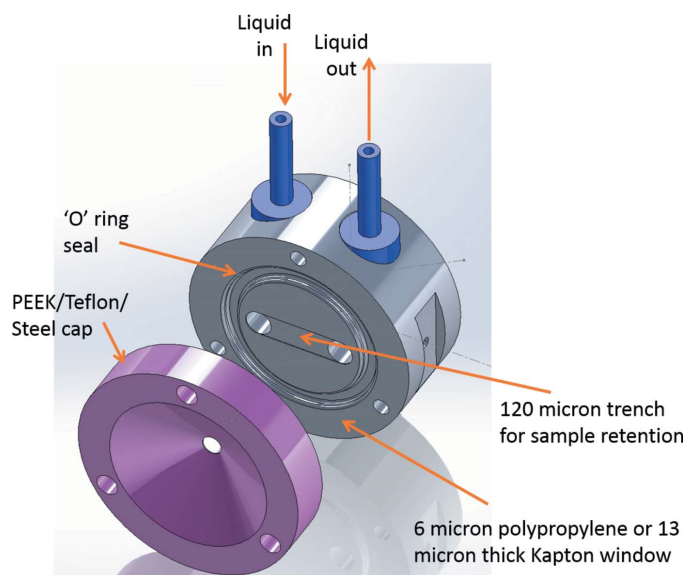
Figure 3
Schematic of the flow cell designed for soft X-ray studies of liquids and liquid–solid chemistry.

position as the flow passed through it was to moisten the powder with some of the solvent to yield a paste that could be spread within the sample area prior to sealing with the window material.

At these low energies the choice of window material is limited. Thus far we have successfully used this cell in this energy regime using windows made of either polypropylene (6 μm thick) or Kapton (13 μm thick). The latter has better mechanical properties and a much higher ultimate temperature of operation. However, the results reported in this paper (see below) all utilized the polypropylene. When using this material, however, it was found that, in order to prevent an outward swelling of the window, bubble formation and the

best retention of the powder sample in the liquid flow, the window should be stretched as much as possible over a slight over-packed sample bed before sealing with the front cap.

In its first use (Sherborne *et al.*, 2015) the stainless steel cap was used successfully to study the Cl K-edge *in situ*. However, and subsequent to the implementation of a more sensitive (KETEK) detector, it was found that, even with harmonic rejection mirrors in place, fluorescence contributions from the stainless steel (arising from a leakage of the third harmonic of the X-rays at *ca.* 10^{-6} of the fundamental that could scatter onto this cap) could be observed to the detriment of the soft X-ray investigation. To resolve this problem the front cap was remade in PEEK and Teflon which effectively resolved this issue.

As will be shown below, this cell may be successfully used to study supported catalysts at, for instance, the Cl K- and Pd L_3-edges under moderate flows (0.1 ml min^{-1}) and to temperatures up to *ca.* 353 K (limited by the solvent mixture used). A second generation of this cell has now been designed and will be implemented in the near future.

In the following, all spectra were collected using the fluorescence detector mounted in plane at 90° to the X-ray beam and with a sample oriented at 45° to the incoming beam. At the highest energy to be interrogated in a scan the total count rate detected was moderated (by translating the monitor and sample detectors to or away from their targets) such that non-linearity in the counting of each detector was avoided and their overall count rates were as similar as possible. Regions of interest were then established for the sample detector depending on the measurement to be made. Individual scans were then set up with energy increments of 0.25 eV for XANES and 2 eV for portions of a scan (EXAFS) lying in between two edges under study. Unless otherwise stated, a counting time of 10 s per point and a focused beam of ~ 0.5 mm^2 was used.
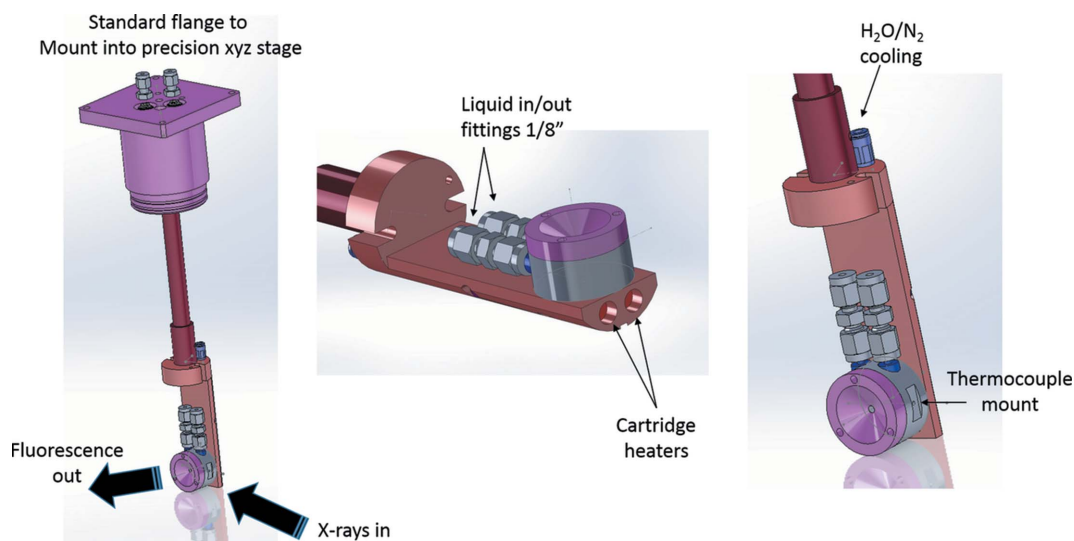
Figure 4
Overall cell assembly showing incorporation of the heating elements and feedthrough system that mounts within the general chamber shown in Fig. 2 and within the six-circle diffractometer at the XMaS beamline.

4. Performance for XAFS in the 2–4 keV range in application to the study of functional materials

4.1. Electronic structure of ionic liquids using the S K-edge

Ionic liquids are an extensively researched and potentially important class of materials in many areas, including electrochemistry and catalysis (Armand et al., 2009; Pârvulescu & Hardacre, 2007). For ionic liquids the electrostatic intermolecular interactions are described by Coulomb's law and hence the atomic charges, q_i, must be elucidated in order to evaluate these interactions (Rigby & Izgorodina, 2013). Amongst their many properties is that, despite most being liquids at room temperature, they exhibit extremely low vapour pressures (similar to alkali metals) and therefore are amenable to study in vacuo (Lovelock et al., 2010). Using X-ray photoelectron spectroscopy, it has been demonstrated that the ionic liquid anion can affect q_i on the cation (Cremer et al., 2010). In addition, EXAFS spectroscopy with hard X-rays has been used to study structure in ionic liquids (Hartley et al., 2014; Migliorati et al., 2015).

We propose that XANES spectroscopy can be used to probe q_i (and charge transfer) in ionic liquid-based materials. Here, we use S K-edge XAFS on the XMaS beamline to assess the effect of the cation on the anion liquid phase electronic structure. We use the S K-edge energy, here labelled E_{NEXAFS}, the energy required to take an electron from a S 1s core level to the first unoccupied molecular orbital located on the sulfur atom. Such studies, as can be seen, require high-quality data with good energy resolution in order to discern changes in electronic structure that can be very subtle.

In these cases the ionic liquids were sufficiently cohesive that they were simply applied to the motorized sample changer described in §3.1. The sample changer was mounted vertically within the general-purpose vacuum chamber and maintained under a vacuum of better than 10^{-6} mbar whilst S K-edge XANES spectra were collected.

To demonstrate the sensitivity of our technique, Fig. 5(a) shows the S K-edge XANES spectra for three solid sodium-based salts (sodium with hydrogensulfate, ethylsulfate and sulfate). E_{XANES} was measurably different for these three solid salts (2481.0 eV, 2481.3 eV, 2481.9 eV), as has been observed for similar potassium salts (Pin et al., 2013).

Fig. 5(b) shows XANES spectra for two ionic liquids, 1-butyl-3-methylimidazolium hydrogensulfate [C$_4$C$_1$Im]- [HSO$_4$] and butyldimethylammonium hydrogensulfate [N$_{4,1,1,0}$][HSO$_4$]. In these cases changing the cation has little effect on the S K-edge spectra. E_{XANES} was the same for both ionic liquids, 2481.0 eV. In addition, the shapes of the XANES spectra are broadly similar, although there are subtle differences.

It must be borne in mind that the [C$_4$C$_1$Im]$^+$ cation and the [N$_{4,1,1,0}$]$^+$ cation are significantly different. [C$_4$C$_1$Im]$^+$ has a delocalized π-system, and the [N$_{4,1,1,0}$]$^+$ cation will hydrogen-bond more strongly to the [HSO$_4$]$^-$ anion than the [C$_4$C$_1$Im]$^+$ cation (Hunt et al., 2015). In spite of these different cations, E_{NEXAFS} is the same within the error of the experiment, demonstrating that the cation has little effect on q_i of the [HSO$_4$]$^-$ anion.

4.2. Studies at the Cl K- and Rh L_3-edges: standards and limits of detection

4.2.1. Some standards at the Cl K- and Rh L_3-edges. Fig. 6(a) shows normalized Cl K-edge XANES from Rh$^{\mathrm{III}}$Cl$_3$ (anhydrous), Rh$^{\mathrm{III}}$Cl$_3$.3H$_2$O and (NH$_4$)$_3$RhCl$_6$. Fig. 6(b) shows the Rh L_3-edge for these standards along with that obtained from Rh$_2^{\mathrm{III}}$O$_3$. The spectra obtained are found to be in good agreement with those recorded previously for the compounds at these edges (Sugiura et al., 1986; Wu & Ellis, 1995).

The Cl K-edge XANES is, in each case, characterized by strong pre-edge features. Cl K-edge pre-edge features may be generically associated with a mixing between the Cl p and transition metal d orbitals and indicative of the degree of covalency in the bonding (Shadle et al., 1995; Neese et al., 1999; Glaser et al., 2000; DeBeer et al., 2008).

In both Rh$^{\mathrm{III}}$Cl$_3$ cases there is evidence of the pre-edge feature being comprised of at least two components. This is most obvious in the case of RhCl$_3$.3H$_2$O where the splitting of ca. 2 eV between the two components is clear. The origins of these shifts in the pre-edge features of the Cl K-edge lie in the possible geometrical variations in ligand placement in an octahedral shell around the Rh$^{\mathrm{III}}$ centre: the relatively sharp feature in the case of (NH$_4$)$_3$Rh$^{\mathrm{III}}$Cl$_6$ is singular as symmetrically all the Cl atoms are equivalent. In the Rh$^{\mathrm{III}}$Cl$_3$.3H$_2$O case the equivalence of the Cl atoms is reduced and a number of isomeric permutations arise that are founded upon Cl existing cis or trans to either other Cl atoms or coordinating water molecules. By reference to (NH$_4$)$_3$Rh$^{\mathrm{III}}$Cl$_6$ we might, to

(a) (b)

Energy (keV)

Normalised absorbance
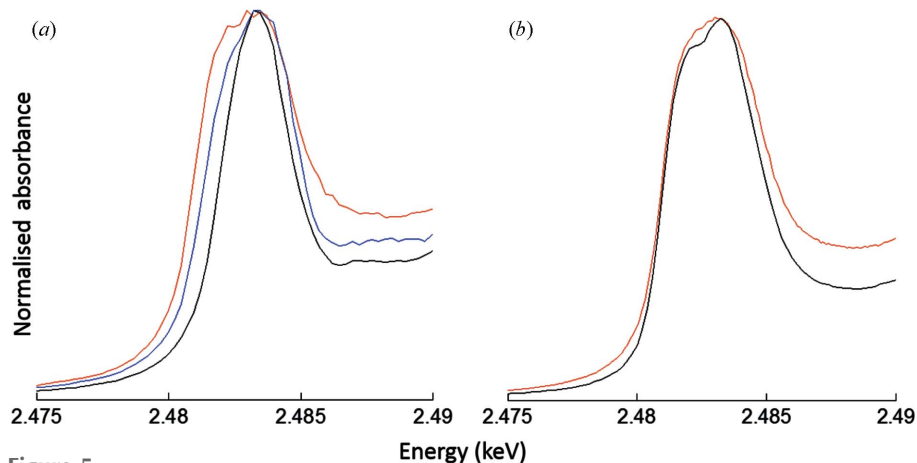
Figure 5
Sulfur K-edge XANES for (a) sodium-based salts [sodium with hydrogensulfate (blue), ethylsulfate (red) and sulfate (black)]; (b) 1-butyl-3-methylimidazolium hydrogensulfate, [C$_4$C$_1$Im][HSO$_4$] (black), and butyldimethylammonium hydrogensulfate, [N$_{4,1,1,0}$][HSO$_4$] (red).
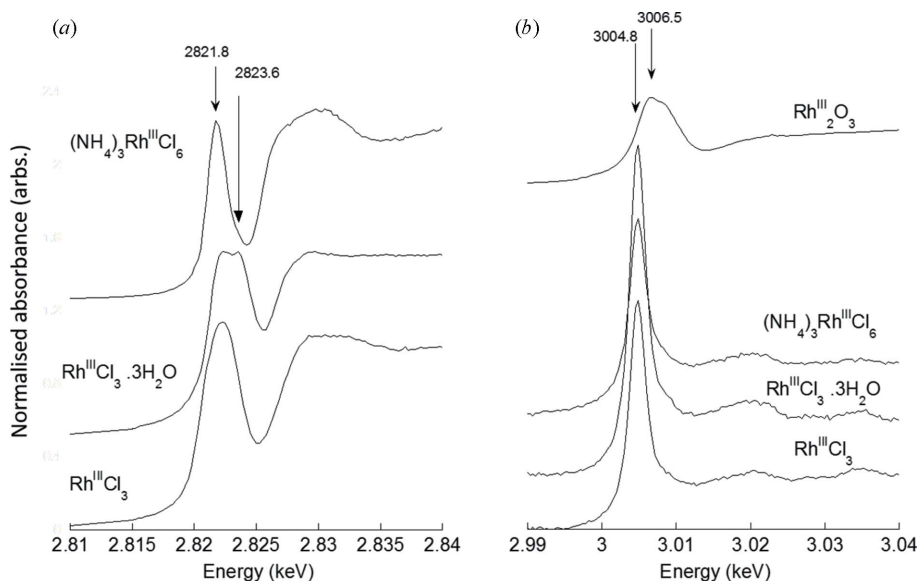
Figure 6
(a) Cl K-edge and (b) Rh L_3-edge XANES derived from four Rh^{III} standards as indicated.

Table 1
Binding energies for Cl K-edge pre-edge features and for the white line maximum at the Rh L_3-edge for a number of standards as indicated.

Sample	Cl K-edge pre-edge (eV)	Rh L_3-edge white line (eV)
$(NH_4)_3Rh^{III}Cl_6$	2821.8	3004.8
$Rh^{III}Cl_3$ (anhydrous)	2822.2	3004.8
$Rh^{III}Cl_3.3H_2O$	2821.6	3004.8
	2823.6	
$Rh_2^{III}O_3$		3006.5
$[Rh^I(CO)_2Cl]_2$	2823.2	3007.0

a first approximation, associate the lowest-energy pre-edge peak to Cl *trans* to Cl and the higher binding energy feature as arising from OH$_2$ *trans* to Cl.

That there is evidence for two components in the anhydrous Rh^{III}Cl$_3$ case most likely stems from adventitious intrusion of some moisture to this system as a result of the mounting of this sample.

Table 1 summarizes the positions of these pre-edge features for each standard along with the energies of the maximal absorbance at the 'white lines' of the Cl K- and Rh L_3-edge found in each Rh$_{III}$ case. The same values for the $[Rh^I(CO_2)Cl]_2$ dimer investigated later on in this paper are also given. Broadly speaking, the shifts in energies of the Cl K-edge pre-edge feature scale in relation to position of the ligands within the spectrochemical series and the anomalously high binding energy of the Rh L_3-edge in the $[Rh^I(CO_2)Cl]_2$ case is most likely also a result of the presence of the strong, p acceptor, CO ligands.

4.2.2. Assessment of dilution limits: the case of Rh^{III}Cl$_3$/H$_2$O. Fig. 7 shows

XANES spectra derived from aqueous solutions of RhCl$_3$. Fig. 7(a) shows the normalized (to a post-edge value of 1) Cl K-edge XANES, Fig. 7(b) the raw absorbance Rh L_3-edges scaled as indicated. Fig. 8 shows the concentrations dependence of the Cl K pre-edge intensity (I) and post-edge (II) features. All spectra were collected at 10 s per point and are single spectra with the exception of those at sub-millimolar concentration that are the average of three scans.

For the Cl K-edge it is evident that XANES useful spectra can be obtained well into the sub-millimolar range. For the Rh L_3-edge the sensitivity of the experiment is less (see below) but the Rh L_3-edge white line can still be addressed and information from it obtained to *ca.* 1 mmol.

Chemically the changes in the Cl K-edge XANES reflect the changing coordination environment of the Rh as the solution is diluted as a result of the exchange of ligands occurring around the octahedral Rh^{III} and the equilibrium between Cl coordination to Rh^{III} centres and as solvated Cl$^-$ ions, *i.e.*

$$Rh^{III}Cl_3(H_2O)_3 \longleftrightarrow Rh^{III}(H_2O)_6 + 3Cl^- \qquad (1)$$
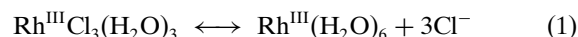
For Rh^I and Rh^{III} electronic configurations orbital mixing between the Cl p and Rh d orbitals may occur resulting in the observed pre-edge feature (Sugiura *et al.*, 1986; Wu & Ellis, 1995); when Cl is present as a solvated ion this orbital mixing cannot occur and therefore the pre-edge feature cannot exist. Correspondingly, the pre-edge feature is replaced by a new post-edge state that reflects the growing predominance of solvated Cl.
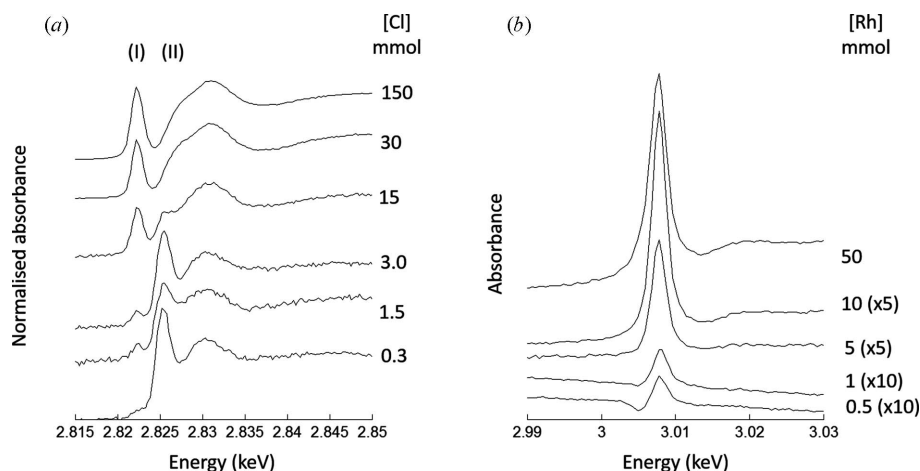
Figure 7
(a) Normalized Cl K-edge XANES and (b) Rh L_3-edge XANES absorbance (not normalized) derived from aqueous RhCl$_3$ solutions as a function of [Cl]. In (b), scaling factors, to aid comparison over the range of concentrations, are given in parentheses.
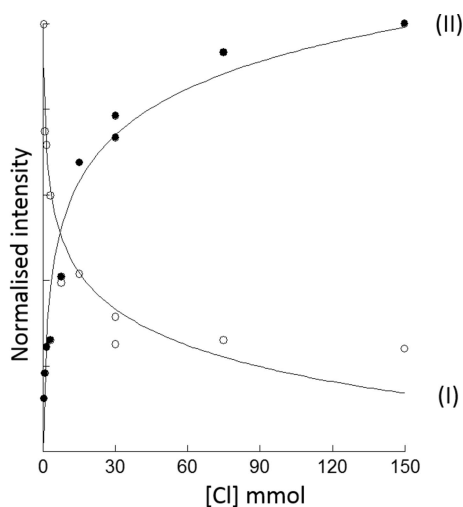
Figure 8
Concentration dependence of the Cl K-edge XANES features (I = pre-edge; II = post edge) as identified in Fig. 7, obtained from aqueous solutions of $Rh^{III}Cl_3$. The fitted curves are logarithmic functions.

The differences in sensitivity between Cl K- and Rh L_3-edges may be seen as a convolution of three effects: differences in excitation cross sections and fluorescence yields of the Cl K- and Rh L_3-edges; the difference in sampling depth at the Rh L_3-edge *versus* the Cl K-edge; the high Cl fluorescence background at the Rh L_3-edge as compared with the Cl K-edge; and, in the current case, the effectiveness of the normalization of the Rh L_3-edge arising from the upstream Rh mirror. At progressively lower concentrations the precision of the normalization at the Rh L_3-edge has to be proportionately more precise (in this sense it is a good test) so as to avoid a breakthrough into the absorbance spectrum of the instrument response in this region. The effectiveness of the current normalization of the contribution from the Rh mirror can be seen (in the raw absorbance spectra) to be compromised around *ca.* 1 mmol Rh in the current setup. Indeed, even more than the total photon flux obtainable from this beamline at these energies, the precision of the normalization process would, in this case, be the limiting factor to the dilutions that we may achieve to study.

At present therefore, and taking the worst case, in terms of the instrument, scenario of the Rh L_3-edge, we can state that, using the XMaS beamline in its current incarnation, we can study chemistry in solution in this 2–4 keV range to at least the level of 1 mmol using XANES. Equally, it is clear for other edges not affected by the instrument response function itself (*i.e.* Cl K-edge) that the lower limit of detection is considerably lower than this and quite comfortably into the micromolar range.

4.3. *In situ* study of gas–solid interactions: metallo-organic chemical vapour deposition (MOCVD) and decomposition of $[Rh^I(CO)_2Cl]_2$ on γ-Al_2O_3

The volatile organo-metallic $[Rh^I(CO)_2Cl]_2$ serves as a useful probe molecule to assess both the Cl K-edge and Rh L_3-edge XAS from a model system that has previously been well studied in terms of the basic chemistry it displays when supported upon metal oxide surfaces and high area supports such as γ-Al_2O_3 (see, for instance, Frederick *et al.*, 1987; Binsted *et al.*, 1989; Evans *et al.*, 1992a,b, 2000; Hayden *et al.*, 1997, 1998, 2001; Newton *et al.*, 2001, 2002, 2006; Bennett *et al.*, 2007; Roscioni *et al.*, 2013).

The chemistry of the supported monomeric $(O)Rh^I(CO)_2Cl$ species is of significant interest in terms of a variety of catalytic reactions and in the oxidative re-dispersion of small Rh particles by CO (Van't Blik *et al.*, 1983; Johnston & Joyner, 1993; Cavers *et al.*, 1999; Suzuki *et al.*, 2003; Newton *et al.*, 2004, 2006; Newton, 2009; Figueroa & Newton, 2014; Dent *et al.*, 2007).

The parent dimer $[Rh^I(CO)_2Cl]_2$ sublimes at temperatures not much above ambient and therefore this molecule is easily dosed into a vacuum. In our case this deposition was to γ-Al_2O_3 powder (Degussa Alu-C) that had been deposited from a suspension in 2-propanol onto a flat Al_2O_3 plate (Goodfellow) and allowed to dry. This in turn was mounted on the Cu stub at the end of the variable-temperature cryostat system previously described and kept *in vacuo* at better than 1×10^{-6} mbar and then cooled to 70 K for deposition of the $[Rh^I(CO)_2Cl]_2$. After measurement the temperature was then incremented and at each temperature the vacuum chamber back-filled with H_2 to *ca.* 1×10^{-2} mbar for 10 min before measuring again. This process was repeated to 623 K before the sample was cooled back to room temperature (RT) and then exposed to CO (1×10^{-2} mbar/10 min).

Fig. 9 shows (*a*) the complete (normalized) spectra recorded at each temperature; (*b*) details of the development of the Cl K-edge XANES; and (*c*) the corresponding Rh L_3-edge data. Fig. 10 then shows (*a*) derivative spectra from the Cl K-edge as a function of temperature, and (*b*) the evolution of the system from other points of view: namely, the stoichiometric Rh/Cl ratio derived from the edge jumps and the intensity at two energies (3004 and 3006 eV) within the Rh L_3-edge envelope.

MOCVD at 70 K leads to the physisorption of the parent dimer that subsequently dissociates to yield monomeric $(O)Rh^I(CO)_2Cl$. This change is signalled by significant changes in the Cl K-edge XANES with the loss of features above the edge and a distinct shift (by *ca.* -0.6 eV) to lower binding energy of the pre-edge feature. Between 273 and 373 K this layer remains largely intact though some evidence of the decomposition of the $(O)Rh^I(CO)_2Cl$ species by 373 K can be detected: the Cl K-edge pre-edge feature continues to attenuate and broaden to lower energy whilst concomitantly the Rh L_3-edge starts to shift to lower energies as well. The latter indicates that the Rh^I complex is starting to decompose to yield Rh^0 nanoparticles and this is accompanied by the commencement of the loss of Cl from to the gas phase (as HCl or Cl_2; online mass spectrometry, not shown).

With further heating this chemistry continues and by 473 K most of the $(O)Rh^I(CO)_2Cl$ monomer has decomposed and the Rh present is predominantly to be found as reduced Rh nanoparticles (this can be seen clearly in the development of post-edge oscillations indicative of Rh–Rh scattering).
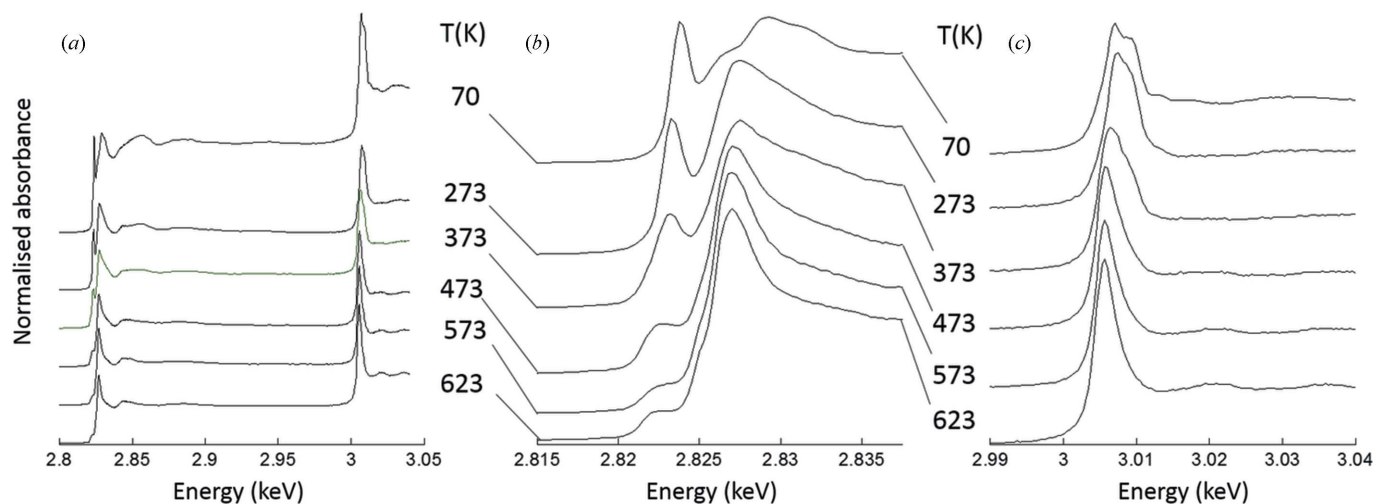
Figure 9
Temperature dependence of Cl K- and Rh L_3-edge XANES derived from in-vacuum MOCVD of $[Rh^I(CO)_2Cl]_2$ to γ-Al_2O_3. At each temperature the sample has been exposed to *ca.* 1×10^{-2} mbar H_2 for 1 min. (*a*) Complete spectra; (*b*) Cl K-edge XANES; (*c*) Rh L_3-edge XANES.
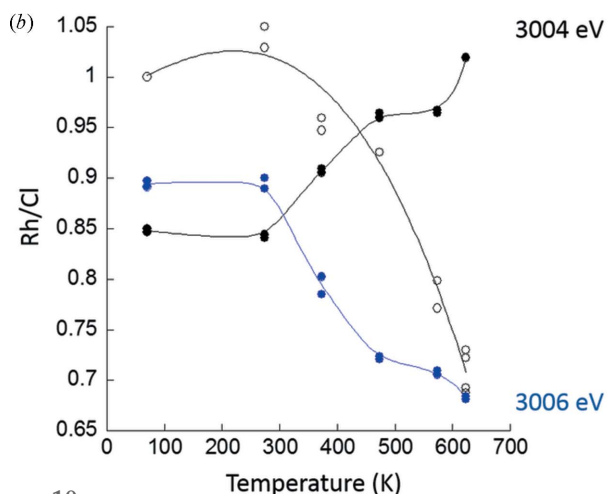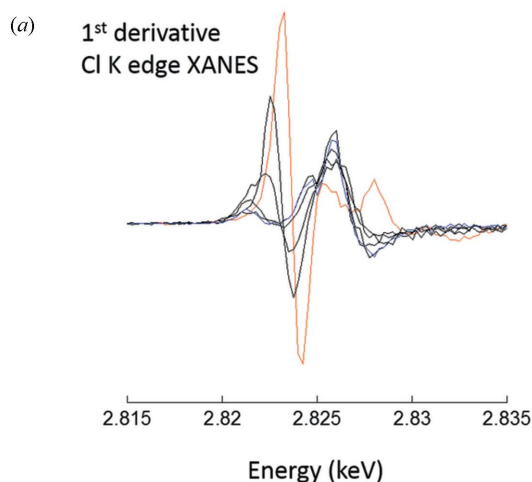
Figure 10
(*a*) First derivative of the normalized Cl K-edge XANES as a function of temperature. The red spectrum is that obtained at 70 K, the blue at 623 K. (*b*) Stoichiometric Rh/Cl ratio as a function of temperature (open circles, left axis) along with the intensity of two features at 3006 eV (blue) and 3004 eV (black) indicative of the starting Rh^I complex and the final nanoparticulate Rh^0.

Notable, however, is the persistence of a good degree of the Cl (even by 623 K only *ca.* 30% of the Cl initially seen to be present has been removed) and that the Cl K pre-edge feature is never observed to disappear completely.

Once the $(O)Rh^I(CO)_2Cl$ has decomposed, the Cl has several potential options open to it: desorb as HCl or Cl_2; bind to Lewis acid sites on the Al_2O_3; or bind to the growing Rh particles. Some (*ca.* 30% by 623 K) clearly desorbs; however, the remainder persists on the surface of the sample.

Given the origins of the Cl K-edge pre-edge feature (Sugiura *et al.*, 1986; Wu & Ellis, 1995; Shadle *et al.*, 1995; Neese *et al.*, 1999; Glaser *et al.*, 2000) and in a manner similar to that observed in the dilution studies using $Rh^{III}Cl_3$, we do not expect any pre-edge feature from Cl bonding to Al centres (no empty d states) or indeed to fully reduced (d band full) Rh surfaces; surface extended X-ray absorption fine structure (SEXAFS) from Cl deposited upon Rh (111), for instance, yields no pre-edge feature (Shard *et al.*, 1999).

The persistence of a small (*ca.* 15% of that observed at 273 K and at lower binding energy) pre-edge feature in the Cl XANES indicates that some fraction of the Cl remains bound to Rh that still displays characteristics of Rh in a higher oxidation state.

The energetic position of the persistent pre-edge feature (*ca.* 2822.3 eV) is more akin to that derived from Rh^{III} reference compounds than it is for the $[Rh^I(CO)_2Cl]_2$ dimer (see Table 1) or the $(O)Rh^ICO_2Cl$ monomer formed by 273 K (2823.3 eV). As such the persistence and binding energy of this feature would seem to indicate that a small portion of the Rh remains bound to the Cl and in a state closer to Rh^{III} than Rh^I or Rh^0. Given the manner in which these samples have been treated we might suggest that this may be indicative of Cl bound at the perimeter of metallic Rh particles where the binding of the Rh to the oxygen of the support may have its strongest effect on the outermost Rh atoms and thus where a binding of the type indicated achievable. Lastly, Fig. 11 shows
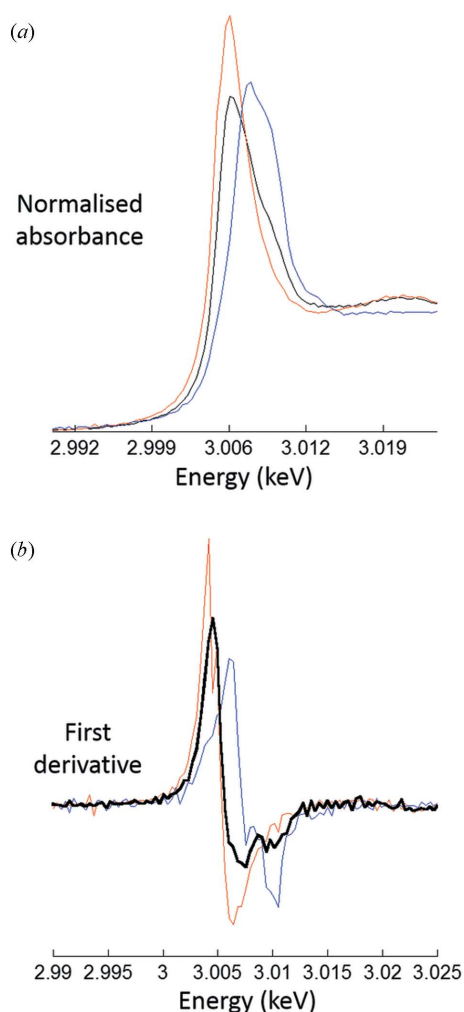
Figure 11
(a) Rh L_3-edge XANES and (b) the first derivatives, from the adsorbed monomer species [(O)Rh^I(CO)$_2$Cl$^-$ blue], a sample reduced to 623 K (red), and that obtained from post-reduction room-temperature exposure to CO (black).

the Rh L_3-edge results from room-temperature exposure of the sample heated to 623 K under H$_2$ to CO.

As has been well documented (Van't Blik *et al.*, 1983; Johnston & Joyner, 1993; Cavers *et al.*, 1999; Suzuki *et al.*, 2003; Newton *et al.*, 2004, 2006; Figueroa & Newton, 2014; Dent *et al.*, 2007), CO regenerates a fraction of the (O)Rh^I(CO)$_2$Cl through an oxidative re-dispersion, though it occurs in this system to only a relatively small degree. This is most likely the result of the Rh particles in this system, having experienced H$_2$ at 623 K, having grown too large for this process to be effective. Nonetheless, the Rh L_3-edge XANES obtained has the sensitivity to detect these relatively small changes.

4.4. Supported Rh-nitrate-derived γ-Al$_2$O$_3$-supported catalysts and Cl contamination in γ-Al$_2$O$_3$

Fig. 12(a) shows Cl K-edge XAFS derived from catalysts made through the wet impregnation of Rh^{III}(NO$_3$)$_3$ (Strem) to a γ-Al$_2$O$_3$ (Degussa Alu-C) and then dried and calcined at 673 K in flowing air. Fig. 12(b) shows details of the Cl K-edge XANES and Fig. 12(c) the Rh L_3-edge XANES.

These spectra, as well as showing the sensitivity of the XAFS experiment in this energy region, reveal something unexpected, *i.e.* that significant levels of Cl are present in each of the catalysts even though there has been no Cl present at any stage of the catalyst preparation.

Fig. 13 shows the Cl K-edge XANES derived from the as-received Al$_2$O$_3$ and compares it with the Cl XANES from the 5 wt% Rh^{III}(NO$_3$)$_3$ derived catalyst. The Cl XANES envelope is very similar, but not equivalent, to that found for the 'Cl-free' catalyst; and in the Rh catalyst case a pre-edge feature, whose intensity scales with the Rh loading, is once again evident. As expected, given the origins of the pre-edge feature in the Cl XANES, this feature is completely absent from the pure Al$_2$O$_3$.

The presence and scaling of the intensity of the pre-edge features in the presence of Rh^{III} in this case shows that some
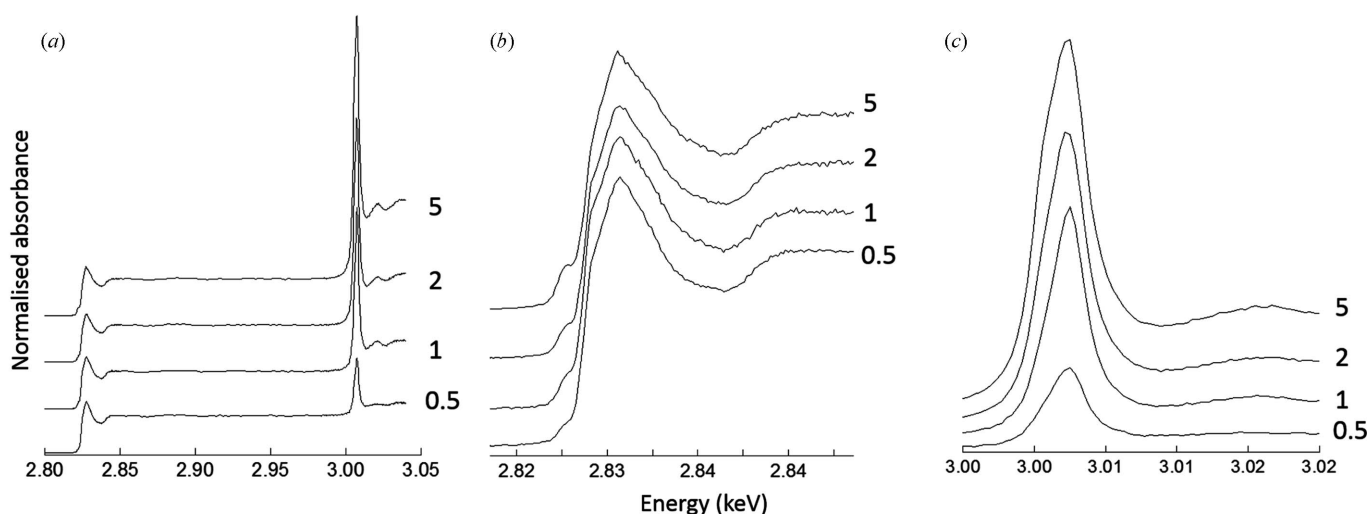
Figure 12
(a) Normalized Cl K-edge and Rh L_3-edge XAFS spectra derived from notionally Cl-free Rh/Al$_2$O$_3$ catalyst samples as a function of Rh loading (5–0.5 wt% as indicated). (b) Close-up of the Cl K-edge region and (c) detail of the Rh L_3-edge.
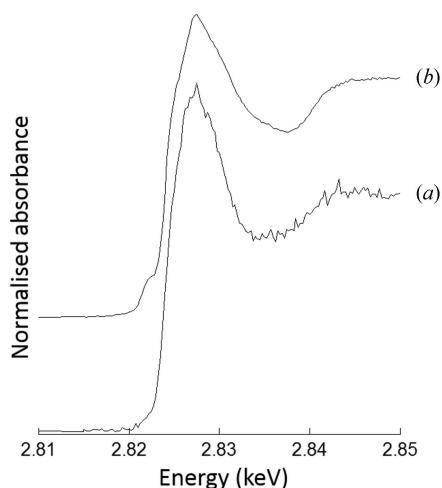
Figure 13
Comparison of Cl K-edge XANES for as-received γ-Al$_2$O$_3$ (Degussa Alu-C) (a) and a calcined 5 wt% Rh^{III}(NO$_3$)$_3$ derived catalyst (b).

of the Rh, that in this case is oxidic in nature (white line at *ca.* 3007.5 eV, Rh^{III}), can react with that proportion of the Cl present in the Al$_2$O$_3$ that is present at the surface of the support.

Whilst other differences in the spectra may well be ascribed to the calcined nature of the Al$_2$O$_3$ in the Rh/Al$_2$O$_3$ catalyst, the pre-edge feature observed in the latter case can only come from the binding of Cl to Rh, in this case in the +3 state. This can only occur through a reaction of the Rh with Cl that exists at the surface of the support and, though this would appear to be a minority component of the overall Cl contaminant, the rest of which we might surmise exists within the Al$_2$O$_3$, it is clearly very significant in terms of the loading of the Rh.

We note that the same Al$_2$O$_3$ was used for the previous study of the decomposition of [Rh(CO)$_2$Cl]$_2$. As such, the retention of an apparent 70% of the Cl initially present in the physisorbed multilayers is revealed as chimeric as we have now observed that this Al$_2$O$_3$ already contains appreciable levels of Cl.

We note that levels of Cl contamination in aluminas is generally quoted at <50 p.p.m., no doubt on the basis of the lower limits of detection of the methods commercially employed to characterize these materials. Additionally, therefore, we have demonstrated that Cl K-edge XAFS on the XMaS beamline is capable of easily detecting Cl contamination at, and considerably beyond, these levels.

Moreover, we can deduce from the spectroscopy shown above, and specifically from the persistence of visible pre-edge components of the Cl K-edge spectra in a notionally Cl-free sample preparation, that a proportion of this Cl is present at the surface of the Al$_2$O$_3$ and may interact with any metals deposited upon it and therefore influence the chemistry subsequently shown by these materials.

4.5. Liquid–solid systems: chlorinated palladium/Al$_2$O$_3$ catalysts interacting with ethanol/H$_2$O solvents mixtures

Having investigated the performance of the XMaS beamline in addressing sulfur speciation in ionic liquids, some

aspects of gas–solid chemistry in supported Rh/Al$_2$O$_3$ catalysts, and Cl speciation occurring within γ-Al$_2$O$_3$, we now consider examples of the application of soft X-ray spectroscopy in the liquid–solid arena. The presence of a liquid phase, with its greatly increased ability to absorb and scatter X-rays compared with a vacuum or gases at low pressure, is a significantly greater challenge in this X-ray energy regime.

As an example we take the sample environment previously described for such studies and apply it to the evolution of a 5% Pd catalyst derived from a Cl precursor upon heating under a 50:50 ethanol–water solvent mixture. Such solvent mixtures have been highlighted as preferable within metrics used to assess the green credentials of solvents preferred as carriers for catalytic reactions for fine chemicals production by the pharmaceutical industry (see, for example, Capello *et al.*, 2007; Henderson *et al.*, 2011). As palladium in many forms is one of the most used catalysts for such conversions, understanding how it might interact with such solvents is of intrinsic interest.

Such a study is, therefore, both a test of our ability to make such measurements but also an attempt to understand the fate of the Cl left within the catalyst as the Pd is reduced. Studies recently made at the Pd K-edge (Brazier *et al.*, 2014) tell us that the use of a Cl precursor has a considerable effect on the kinetics of the reduction of the supported Pd phase. However, study at the Pd K-edge yields no information as to how this might occur or, if Cl is even retained in the starting catalyst, whether it persists within flowing solutions or is leached away. Fig. 14 shows raw absorbance data from such a catalyst (5 wt% Pd/Al$_2$O$_3$) derived from a PdCl$_2$ precursor that has subsequently been dried and then calcined in flowing air at 673 K.
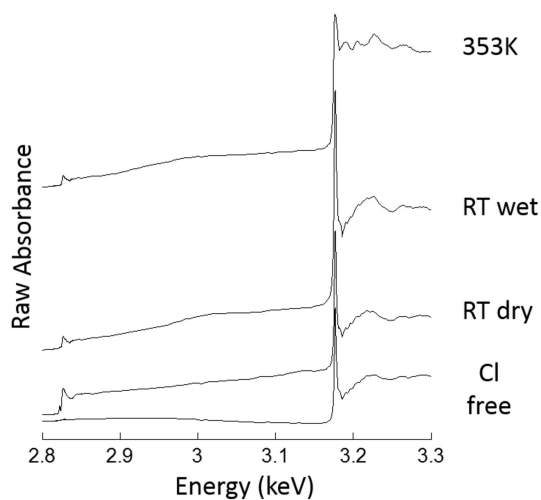
Figure 14
Raw absorbance data for the Cl K- and Pd L_3-edge derived from 5 wt% Pd/Al$_2$O$_3$ catalysts. The bottom spectrum is that derived from a dry catalyst derived from a chlorine-free precursor. Above this is the equivalent dry spectrum from a PdCl$_2$-derived catalyst stuck onto carbon tape and measured in flowing He at RT. This catalyst is then shown having been made 'wet' in the solvent (EtOH:H$_2$O 50:50) within the sample environment previously outlined. The top spectrum is that recorded after heating this catalyst under the flowing (0.1 ml min^{-1}) solvent mixture to 353 K.

As we have already seen, γ-Al$_2$O$_3$ can suffer from significant Cl contamination and therefore the chlorinated sample is also compared (as indicated) in its dry state with a similarly loaded Pd^{II}(NO$_3$)$_2$ derived sample; in this case, however, the γ-Al$_2$O$_3$ used to support the Pd shows barely any evidence of intrinsic Cl contamination.

Two effects of the liquid phase may be intuited from the raw spectra. The first is an apparent change in the Cl/Pd ratio; the second is the presence of increased backgrounds as one proceeds across the energy range investigated. Both these observations may be ascribed to the differentials in the incoming and outgoing fluorescent X-rays to penetrate both the liquid and the solid under study as one moves from 2.7 to 3.3 keV.

Fig. 15 then shows normalized Cl K- and Pd L_3-edge spectra extracted from the data shown in Fig. 14. The normalized data show the poorer statistics obtained at the Cl K-edge as a result of the attenuation of both incident X-rays and Cl K-edge fluorescence as compared with a He environment; this is much less the case for the Pd L_3-edge as a result of both the higher incoming X-ray energies and that of the outgoing Pd L_3-edge fluorescence.

Nonetheless, it can be seen that the Cl is not leached from the catalyst sample by the solvent mixture and persists within the system even as the Pd, originally present as nanosize PdO, is reduced to metallic Pd nanoparticles by the flowing solvent, *i.e.* the same result as obtained from the Pd K-edge studies of this process.

Interestingly, we can also see that the Cl K-edge envelope does change through the process of wetting and then heating the sample. This is most evident in the shift and eventual disappearance of the Cl K-edge pre-edge feature as the sample is made wet and then as it is heated to 353 K under the solvent flow. As the pre-edge feature can only arise from Cl directly attached to Pd in a higher oxidation state, this indicates that, upon wetting, a significant proportion of that Cl is

displaced toward the Al$_2$O$_3$ where its bonding precludes the formation of the state that yields the pre-edge feature.

Aside from this, though the overall shape of the Cl K-edge envelope remains similar throughout the experiment, additional structure is evident from the moment that the sample is made wet. At present the source of these features is unknown though it seems unlikely that they are a result of containment within the sample environment and, for instance, the presence of the 5 µm-thick window required to retain the flowing liquid.

Nevertheless, this demonstrates that the current performance of the XMaS beamline in this energy regime, and the sample environment developed thus far, is sufficient to address problems of this nature and sensitive enough to yield information regarding what is a relatively low level of Cl retention in this catalyst system. Indeed, this approach has already been used to better understand the deactivation of resin-supported Ir(Cp)Cl$_2$ catalysts in the presence of a potassium-containing base through *operando* measurement of the Cl and K K-edges under conditions of catalysis (Sherbourne *et al.*, 2015).

5. Conclusions

We have made a systematic study of the performance of the XMaS beamline at the ESRF for *in situ* XAFS studies on prototypical supported catalysts (containing Rh, Pd and Cl) and ionic liquids containing sulfur. This work shows that a variety of upgrades to the XMaS beamline made, in the first instance, to facilitate low-energy magnetic scattering measurements at the U M_5-edge (3.55 keV), have resulted in a resource that may equally and effectively be used for XANES studies of chemically important materials.

We have assessed the current limitations to sensitivity of the XMaS beamline at the Cl K- and Rh L_3-edges and find that these lie around (Rh L_3) and significantly below (Cl K) the millimolar level. Indeed, we have inadvertently been able to show that certain commercially available γ-aluminas suffer from intrinsic Cl contamination that may be significant in terms of the loadings of transition metals used in many catalyst formulations. Further, we have obtained evidence, from the Cl K-edge pre-edge structure, that significant levels of this Cl may exist at the surface of these aluminas and therefore be able to influence the development and chemistry of any catalytically active elements deposited upon these supports.

Lastly we have outlined experimental resources thus far developed to facilitate *in situ* studies of gas–solid and liquid–solid catalysis and shown that these, in combination with the X-ray optical and X-ray detection resources available at XMaS, may be successfully used to make catalytically relevant, and
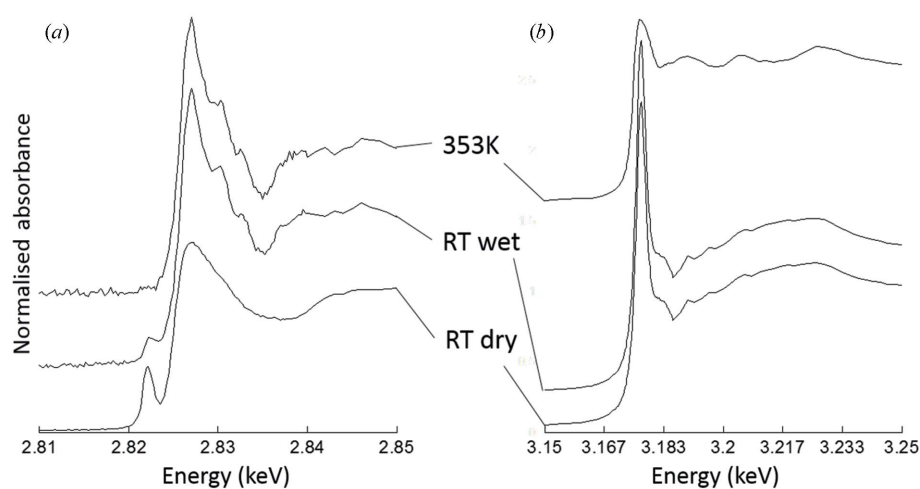
Figure 15
(*a*) Normalized Cl K-edge XANES for a 5 wt% Pd/Al$_2$O$_3$ catalyst derived from a PdCl$_2$ precursor; and (*b*) the corresponding Pd L_3-edge spectra. As previously, spectra are shown for the dry (in He) powder catalyst, that made wet by the flowing solvent at RT, and that obtained after heating *in situ* to 353 K under flowing ethanol–water.

in the liquid–solid case currently unique, measurements in the 2–4 keV region of the X-ray spectrum.

References

Armand, M., Endres, F., MacFarlane, D. R., Ohno, H. & Scrosati, B. (2009). *Nat. Mater.* **8**, 621–629.

Bennett, R. A., McCavish, N. D., Basham, M., Dhanak, V. & Newton, M. A. (2007). *Phys. Rev. Lett.* **98**, 056102.

Binsted, N., Evans, J., Greaves, G. N. & Price, R. J. (1989). *Organometallics*, **8**, 613–620.

Bolin, T. B., Wu, T., Schweitzer, N., Lobo-Lapidus, R., Kropf, A. J., Wang, H., Hu, Y., Miller, J. T. & Heald, S. M. (2013). *Catal. Today*, **205**, 141–147.

Brazier, J. B., Nguyen, B. N., Adrio, L. A., Barreiro, E. M., Leong, W. P., Newton, M. A., Figueroa, S. J. A., Hellgardt, K. & Hii, K. K. (2014). *Catal. Today*, **229**, 95–103.

Brown, M. A., Huthwelker, T., Beloqui Redondo, A., Janousch, M., Faubel, M., Arrell, C. A., Scarongella, M., Chergui, M. & van Bokhoven, J. A. (2012). *J. Phys. Chem. Lett.* **3**, 231–235.

Brown, S. D., Bouchenoire, L., Bowyer, D., Kervin, J., Laundy, D., Longfield, M. J., Mannix, D., Paul, D. F., Stunault, A., Thompson, P., Cooper, M. J., Lucas, C. A. & Stirling, W. G. (2001). *J. Synchrotron Rad.* **8**, 1172–1181.

Capello, C., Fischer, U. & Hungerbühler, K. (2007). *Green Chem.* **9**, 927–934.

Cavers, M., Davidson, J. M., Harkness, I. R., Rees, L. V. C. & McDougall, G. S. (1999). *J. Catal.* **188**, 426–430.

Cremer, T., Kolbeck, C., Lovelock, K. J., Paape, N., Wölfel, R., Schulz, P. S., Wasserscheid, P., Weber, H., Thar, J., Kirchner, B., Maier, F. & Steinrück, H. P. (2010). *Chem. Eur. J.* **16**, 9018–9033.

Dathe, H., Jentys, A. & Lercher, J. A. (2005). *J. Phys. Chem. B*, **109**, 21842–21846.

DeBeer, George, S., Petrenko, T. & Neese, F. (2008). *Inorg. Chim. Acta*, **361**, 965–972.

Del Rio, M. S. & Dejus, R. J. (2004). *AIP Conf. Proc.* **705**, 784–787.

Dent, A. J., Evans, J., Fiddy, S. G., Jyoti, B., Newton, M. A. & Tromp, M. (2007). *Angew. Chem. Intl Ed.* **46**, 5356–5358.

Eerden, A. M. J. van der, van Bokhoven, J. A., Smith, A. D. & Koningsberger, D. C. (2000). *Rev. Sci. Instrum.* **71**, 3260–3266.

Evans, J., Hayden, B., Mosselmans, F. & Murray, A. (1992*a*). *J. Am. Chem. Soc.* **114**, 6912–6913.

Evans, J., Hayden, B., Mosselmans, F. & Murray, A. (1992*b*). *Surf. Sci.* **279**, L159–L164.

Evans, J., Hayden, B. E. & Newton, M. A. (2000). *Surf. Sci.* **462**, 169–180.

Figueroa, S. J. A. & Newton, M. A. (2014). *J. Catal.* **312**, 69–77.

Frederick, B. G., Apai, G. & Rhodin, T. N. (1987). *J. Am. Chem. Soc.* **109**, 4797–4803.

Fulton, J. L., Balasubramanian, M., Pham, V.-T. & Deverman, G. S. (2012). *J. Synchrotron Rad.* **19**, 949–953.

Ghigna, P. & Spinolo, G. (2015). *Sci. Adv. Mater.* **7**, 1–18.

Glaser, T., Hedman, B., Hodgson, K. O. & Solomon, E. I. (2000). *Acc. Chem. Res.* **33**, 859–868.

Hartley, J. M., Ip, C. M., Forrest, G. C. H., Singh, K., Gurman, S. J., Ryder, K. S., Abbott, A. P. & Frisch, G. (2014). *Inorg. Chem.* **53**, 6280–6288.

Hartman, R. L., McMullen, J. P. & Jensen, K. F. (2011). *Angew. Chem. Intl Ed.* **50**, 7502–7519.

Hayden, B. E., King, A. & Newton, M. A. (1997). *Chem. Phys. Lett.* **269**, 485–488.

Hayden, B. E., King, A. & Newton, M. A. (1998). *Surf. Sci.* **397**, 306–313.

Hayden, B. E., King, A., Newton, M. A. & Yoshikawa, N. (2001). *J. Mol. Catal. A*, **167**, 33–46.

Hayter, C. E., Evans, J., Corker, J. M., Oldman, R. J. & Williams, B. P. (2002). *J. Mater. Chem.* **12**, 3172–3177.

Henderson, R. K., Jiménez-González, C., Constable, D. J. C., Alston, S. R., Inglis, G. G. A., Fisher, G., Sherwood, J., Binks, S. P. & Curzons, A. D. (2011). *Green Chem.* **13**, 854–862.

Hunt, P. A., Ashworth, C. R. & Matthews, R. P. (2015). *Chem. Soc. Rev.* **44**, 1257–1288.

Isaacs, E. D., McWhan, D. B., Peters, C., Ice, G. E., Siddons, D. P., Hastings, J. B., Vettier, C. & Vogt, O. (1989). *Phys. Rev. Lett.* **62**, 1671–1674.

Johnston, P. & Joyner, R. W. J. (1993). *Faraday Trans.* **89**, 863–864.

König, C. F. J., Schuh, P., Huthwelker, T., Smolentsev, G., Schildhauer, T. J. & Nachtegaal, M. (2014). *Catal. Today*, **229**, 56–63.

Ley, S. V. (2012). *Chem. Rec.* **12**, 378–390.

Lovelock, K. R. J., Villar-Garcia, I. J., Maier, F., Steinrück, H. P. & Licence, P. (2010). *Chem. Rev.* **110**, 5158–5190.

Migliorati, V., Serva, A., Aquilanti, G., Olivi, L., Pascarelli, S., Mathon, O. & D'Angelo, P. (2015). *Phys. Chem. Chem. Phys.* **17**, 2464–2474.

Neese, F., Hedman, B., Hodgson, K. O. & Solomon, E. I. (1999). *Inorg. Chem.* **38**, 4854–4860.

Newman, S. G. & Jensen, K. F. (2013). *Green Chem.* **15**, 1456–1472.

Newton, M. A. (2009). *Top. Catal.* **52**, 1410–1424.

Newton, M. A., Burnaby, D. G., Dent, A. J., Diaz-Moreno, S., Evans, J., Fiddy, S. G., Pascarelli, S. & Turin, S. (2001). *J. Phys. Chem. A*, **105**, 5965–5970.

Newton, M. A., Burnaby, D. G., Dent, A. J., Diaz-Moreno, S., Evans, J., Fiddy, S. G., Neisius, T. & Turin, S. (2002). *J. Phys. Chem. B*, **106**, 4214–4222.

Newton, M. A., Dent, A. J., Diaz-Moreno, S., Fiddy, S. G., Jyoti, B. & Evans, J. (2006). *Chem. Eur. J.* **12**, 1975–1985.

Newton, M. A., Jyoti, B., Dent, A. J., Fiddy, S. G. & Evans, J. (2004). *Chem. Commun.* pp. 2382–2383.

Nurk, G., Huthwelker, T., Braun, A., Ludwig, C., Lust, E. & Struis, R. P. W. J. (2013). *J. Power Sources*, **240**, 448–457.

Pârvulescu, V. I. & Hardacre, C. (2007). *Chem. Rev.* **107**, 2615–2665.

Paul, D. F., Cooper, M. J. & Stirling, W. G. (1995). *Rev. Sci. Instrum.* **66**, 1741–1744.

Pin, S., Huthwelker, T., Brown, M. A. & Vogel, F. J. (2013). *J. Phys. Chem. A*, **117**, 8368–8376.

Rigby, J. & Izgorodina, E. I. (2013). *Phys. Chem. Chem. Phys.* **15**, 1632–1646.

Roscioni, O. M., Dyke, J. M. & Evans, J. (2013). *J. Phys. Chem. C*, **117**, 19464–19470.

Shadle, S. E., Hedman, B., Hodgson, K. O. & Solomon, E. I. (1995). *J. Am. Chem. Soc.* **117**, 2259–2272.

Shard, A. G., Dhanak, V. R. & Santoni, A. (1999). *Surf. Sci.* **429**, 279–286.

Sherborne, G. J., Chapman, M., Blacker, J. A., Bourne, R., Chamberlain, T., Crossley, B., Lucas, S., McGowan, P., Newton, M. A., Screen, T., Thompson, P., Willans, C. & Nguyen, B. N. (2015). *J. Am. Chem. Soc.* **137**, 4151–4157.

Sugiura, C., Kitamura, M. & Muramatsu, S. (1986). *J. Chem. Phys.* **84**, 4824–4827.

Suzuki, A., Inada, Y., Yamaguchi, A., Chihara, T., Yuasa, M., Nomura, M. & Iwasawa, Y. (2003). *Angew. Chem. Intl. Ed.* **42**, 4795–4799.

Tamenori, Y. (2010). *J. Synchrotron Rad.* **17**, 243–249.

Tamenori, Y. (2013). *J. Synchrotron Rad.* **20**, 419–425.

Tamenori, Y., Morita, M. & Nakamura, T. (2011). *J. Synchrotron Rad.* **18**, 747–752.

Thompson, P. B. J., Brown, S. D., Bouchenoire, L., Paul, D. F., Mannix, D., Normile, P. S., Bikondoa, O., Hase, T., Kervin, J., Lucas, C. A., Cooper, M. J., Garrett, R., Gentle, I., Nugent, K. & Wilkins, S. (2010). *AIP Conf. Proc.* **1234**, 407–410.

Van't Blik, H. F. J., Van Zon, J. B. A. D., Huizinga, T., Vis, J. C., Koningsberger, D. C. & Prins, R. (1983). *J. Phys. Chem.* **87**, 2264–2267.

Wu, Y. & Ellis, D. E. (1995). *J. Phys. Condens. Matter*, **7**, 3973–3989.